



# Fabrication of a novel p-n heterojunction photocatalyst n-BiVO<sub>4</sub>@p-MoS<sub>2</sub> with core–shell structure and its excellent visible-light photocatalytic reduction and oxidation activities

Wei Zhao <sup>a</sup>, Ying Liu <sup>a</sup>, Zhongbo Wei <sup>a</sup>, Shaogui Yang <sup>a,\*,\*\*</sup>, Huan He <sup>a,b</sup>, Cheng Sun <sup>a,\*</sup>

<sup>a</sup> State Key Laboratory of Pollution Control and Resource Reuse, School of the Environment, Nanjing University, Nanjing 210023, PR China

<sup>b</sup> School of Public Health, University of Illinois at Chicago, Chicago, IL 60631, United States

## ARTICLE INFO

### Article history:

Received 27 September 2015

Received in revised form 4 December 2015

Accepted 11 December 2015

Available online 15 December 2015

### Keywords:

n-BiVO<sub>4</sub>@p-MoS<sub>2</sub>

p-n heterojunction photocatalyst

Core–shell

Photocatalytic mechanism

## ABSTRACT

The novel p-n heterojunction photocatalyst n-BiVO<sub>4</sub>@p-MoS<sub>2</sub> with core–shell structure was successfully fabricated for the first time through a facile in-situ hydrothermal method, in which MoS<sub>2</sub> shell thickness was easily tuned by varying the concentration of MoS<sub>2</sub> precursor in the solution. The photocatalytic performances of samples were systematically investigated via the photocatalytic reduction of Cr<sup>6+</sup> and oxidation of crystal violet (CV) under visible-light irradiation. The BiVO<sub>4</sub>@MoS<sub>2</sub> samples exhibited excellent photocatalytic performance, among which, the BiVO<sub>4</sub>@MoS<sub>2</sub> (10 wt%) sample with MoS<sub>2</sub> shell 300 nm thickness, showed the highest photoreduction and photooxidation activities. The enhanced photocatalytic activities could be attributed to the suppression of charge recombination, the high specific surface area and strong adsorption ability toward the pollutant molecule, and the enhanced or tunable light absorption of BiVO<sub>4</sub>@MoS<sub>2</sub>. Especially, the core–shell structure geometry also increases the contact area between BiVO<sub>4</sub> and MoS<sub>2</sub>, which facilitates the charge transfer at the BiVO<sub>4</sub>/MoS<sub>2</sub> interface. The photocatalytic mechanism of BiVO<sub>4</sub>@MoS<sub>2</sub> for reduction of Cr<sup>6+</sup> and oxidation of CV was discussed in detail. Moreover, 12 photocatalytic degradation intermediates and products of CV were also identified by the gas chromatography–mass spectrometer (GC-MS).

© 2015 Elsevier B.V. All rights reserved.

## 1. Introduction

In the past few decades, photocatalyst has been used extensively to deal with energy and environmental problems, such as solar energy conversion and pollutant removal. The catalytic performance of many wide band gap ( $E_g$ ) photocatalysts is limited to UV light radiation, which is only 3–5% of solar radiation. To better use the solar light for energy conversion, the development of visible-light-responsive photocatalysts is highly desirable because visible-light contributes about 43% to the solar spectrum. Therefore, numerous new photocatalysts with appropriate and small band gap have been designed and explored to make full use of the solar energy [1–3]. Particularly, since Zou et al. [4] reported direct splitting of water under visible-light irradiation with new types of oxide semiconductor photocatalyst, visible-light-driven photocat-

alyst has become one of the hot spots in the field of photocatalysis research [5–7].

Recently, monoclinic scheelite bismuth vanadate (BiVO<sub>4</sub>) with a medium  $E_g$  of about 2.4 eV has received much attention owing to its unique properties, such as ferroelasticity, ionic conductivity, gas sensing, and coloristic properties [8–11]. Moreover, it is also considered as a promising visible-light-driven photocatalyst due to its excellent visible-light response, chemical stability, nontoxicity as well as relatively high photocatalytic activity for water splitting and degradation of organic compounds [12–14]. However, the photocatalytic activity of BiVO<sub>4</sub> is still low owing to its poor capability to separate electron–hole pairs, small specific surface area and weak surface adsorption ability [15–17]. Thus, further study is necessary to enhance its performance for practical application.

As an efficient method to improve photocatalytic properties, heterojunction photocatalysts are used to facilitate the separation of photoexcited electron–hole pairs [18–20]. To enhance the photocatalytic activity of pure BiVO<sub>4</sub>, a number of BiVO<sub>4</sub>-based heterojunction photocatalysts, such as CaFe<sub>2</sub>O<sub>4</sub>/BiVO<sub>4</sub> [21], BiVO<sub>4</sub>/Bi<sub>4</sub>V<sub>2</sub>O<sub>11</sub> [22], Ag<sub>3</sub>PO<sub>4</sub>/BiVO<sub>4</sub> [23], etc., have been conducted in the past decades. For example, Li et al. have successfully

\* Corresponding author. Fax: +86 25 89680580.

\*\* Corresponding author.

E-mail addresses: [yangsg@nju.edu.cn](mailto:yangsg@nju.edu.cn) (S. Yang), [envidean@nju.edu.cn](mailto:envidean@nju.edu.cn), [philasun@126.com](mailto:philasun@126.com) (C. Sun).

constructed an efficient g-C<sub>3</sub>N<sub>4</sub>/BiVO<sub>4</sub> heterojunction photocatalyst, which shows superior visible-light photocatalytic activities in degradation of methylene blue [24]. Gao et al. have synthesized novel heterostructured BiVO<sub>4</sub>/Bi<sub>2</sub>S<sub>3</sub> hollow nano-discoid with mesoporous shell by a facile anion exchange approach, the as-obtained heterostructured BiVO<sub>4</sub>/Bi<sub>2</sub>S<sub>3</sub> hollow discoid exhibits superior photocurrent response and photocatalytic activity for reduction of Cr<sup>6+</sup> under visible-light illumination [25]. These results reveal that coupling two semiconductor photocatalysts with different and matched energy levels is an ideal approach to achieve efficient charge separation, thus the performance of heterojunction photocatalyst is better than that of single one.

More recently, two-dimensional (2D) nanosheets have been attracting considerable attention due to their unique structural, electronic, and optical properties. Among these 2D-layered materials, MoS<sub>2</sub>, composed of Mo atoms sandwiched between two layers of hexagonally close-packed sulfur atoms has been widely studied in the field of photocatalysis because of its high specific surface area and strong surface adsorption ability [26,27]. For example, Zhou et al. have fabricated the few-layer MoS<sub>2</sub> nanosheet coated TiO<sub>2</sub> nanobelts via a hydrothermal reaction, which possesses high specific surface area and strong adsorption ability toward organic dyes and shows excellent photoactivity in hydrogen production and rhodamine B (RhB) degradation [28]. Li et al. reported that the flower-like MoS<sub>2</sub>/BiVO<sub>4</sub> composite with heterojunction showed excellent performance for photodegradation of methylene blue. The authors ascribed the enhanced performance to the staggered band alignment formed between MoS<sub>2</sub> and BiVO<sub>4</sub> [29]. These studies have demonstrated that 2D-layered MoS<sub>2</sub> has immense potential in the field of photocatalysis. However, MoS<sub>2</sub> has some disadvantages such as insufficient charge separation and poor charge mobility [30], both of which lead to low photocatalytic activity. Therefore, enhancing the photocatalytic activity of MoS<sub>2</sub> needs further study.

From the foregoing discussion, it is hypothesized that the highly efficient photocatalyst may be achieved by taking advantage of the efficient charge transfer of heterojunction and the high specific surface area and strong adsorption ability of 2-D MoS<sub>2</sub> nanosheets. To test this hypothesis, the novel and unique 2D MoS<sub>2</sub> nanosheet-coated BiVO<sub>4</sub> decahedron heterojunction photocatalysts have been elaborated for the first time via a hydrothermal method in this study. Such a 3D hierarchical structure consists of a core of BiVO<sub>4</sub> decahedron and shell of MoS<sub>2</sub> nanosheets (referred to as BiVO<sub>4</sub>@MoS<sub>2</sub>). Moreover, MoS<sub>2</sub> is a p-type semiconductor, and BiVO<sub>4</sub> is an n-type semiconductor. Theoretically, a p-n heterojunction will be formed when the p-type MoS<sub>2</sub> and the n-type BiVO<sub>4</sub> combine. The p-n heterojunction could provide a potential driving force, due to the building of an internal electricfield, with its field direction from the n-type to the p-type semiconductor. However, to our knowledge, the preparation and properties of the p-n heterojunction photocatalyst BiVO<sub>4</sub>@MoS<sub>2</sub> with core-shell structure have not yet been reported. This novel system might have potential advantages, such as the improvement of the photogenerated electron-hole separation, the high specific surface area and strong adsorption ability toward the pollutant molecule, and the enhanced or tunable light absorption of BiVO<sub>4</sub>@MoS<sub>2</sub>. Especially, The core-shell structure geometry will also increase the contact area between n-BiVO<sub>4</sub> and p-MoS<sub>2</sub>. The increased contact area will promote the charge transfer at the BiVO<sub>4</sub>/MoS<sub>2</sub> interface.

In the study, p-n heterojunction photocatalyst with core-shell structure was synthesized by a facile hydrothermal coating of MoS<sub>2</sub> against acidic etching BiVO<sub>4</sub> decahedron. Importantly, the MoS<sub>2</sub> shell thickness of 80–300 nm in the core-shell structure can be easily tuned by varying the concentration of MoS<sub>2</sub> precursor (Na<sub>2</sub>MoO<sub>4</sub> and C<sub>2</sub>H<sub>5</sub>NS) in the solution during the hydrothermal

process. This facile synthesis strategy for the p-n heterojunction photocatalyst BiVO<sub>4</sub>@MoS<sub>2</sub> is schematically depicted in Fig. 1.

Benefiting from the unique structural features, the photocatalytic performance of as-obtained the p-n heterojunction photocatalyst BiVO<sub>4</sub>@MoS<sub>2</sub> was investigated via the photocatalytic reduction of Cr<sup>6+</sup> and oxidation of crystal violet (CV) under visible-light irradiation. The catalytic mechanism of the p-n heterojunction photocatalyst BiVO<sub>4</sub>@MoS<sub>2</sub> was discussed in detail. The in-situ hydrothermal synthetic strategy may open a new opportunity to develop highly efficient visible-light-driven p-n heterojunction photocatalyst for environmental applications.

## 2. Experimental

### 2.1. Materials

Bismuth nitrate hydrate (Bi(NO<sub>3</sub>)<sub>3</sub>·5H<sub>2</sub>O), ammonium metavanadate (NH<sub>4</sub>VO<sub>3</sub>), sodium molybdate (Na<sub>2</sub>MoO<sub>4</sub>·2H<sub>2</sub>O), thioacetamide (C<sub>2</sub>H<sub>5</sub>NS) and other chemicals used in the experiments were of analytically pure grade (99%). These chemicals were purchased from Shanghai Chemical Reagent Ltd., without further purification. Deionized water was used throughout this study.

### 2.2. Preparation of BiVO<sub>4</sub>

The monoclinic BiVO<sub>4</sub> sample was synthesized by a facile hydrothermal process as previously reported [12]. NH<sub>4</sub>VO<sub>3</sub> (12 mmol) and Bi(NO<sub>3</sub>)<sub>3</sub>·5H<sub>2</sub>O (12 mmol) were mixed in 100 mL HNO<sub>3</sub> (2.0 M) solution and subjected to ultrasonication for 10 min, then the pH value of the solution was adjusted to about 2.0 with ammonia solution under stirring until formation of a yellow precipitate. After about 2 h aging, the precipitate at the bottom of the beaker was then transferred into a Teflon-lined stainless steel autoclave and heat treated at 200 °C for 24 h. The sample was allowed to cool to room temperature, and filtrated through a filter paper. The yellow powder was washed with deionized water for 5 times and then dried under vacuum at 80 °C for overnight. The acid treated BiVO<sub>4</sub> was prepared as follows. The as-obtained BiVO<sub>4</sub> sample was added into a Teflon-lined stainless steel autoclave, and filled with HNO<sub>3</sub> (0.02 M) aqueous solution up to 30% of the total volume and maintained at 100 °C for 10 h. Finally, the sample was isolated from the solution by centrifugation and sequentially washed with deionized water for 5 times and then dried under vacuum at 80 °C for 6 h.

### 2.3. Preparation of p-n heterojunction photocatalyst BiVO<sub>4</sub>@MoS<sub>2</sub>

The p-n heterojunction photocatalyst BiVO<sub>4</sub>@MoS<sub>2</sub> (with 2 wt% of MoS<sub>2</sub>) was prepared via in-situ hydrothermal method. Sodium molybdate (Na<sub>2</sub>MoO<sub>4</sub>·2H<sub>2</sub>O, 2.4 mg) and thioacetamide (C<sub>2</sub>H<sub>5</sub>NS, 4.8 mg) were dissolved in 40 mL deionized water and stirred vigorously for 30 min. Then, the acid treated BiVO<sub>4</sub> powder (40 mg) was added into the above solution under vigorous stirring. The solution was transferred into a Teflon-lined stainless steel autoclave and reacted at 200 °C for 24 h. The product was obtained after centrifugation and dried at 80 °C for 12 h. The other samples BiVO<sub>4</sub>@MoS<sub>2</sub> (with 5, 10, 20 wt% of MoS<sub>2</sub>) were also synthesized by the above procedure, and the different content of MoS<sub>2</sub> can be achieved by adjusting the amount of Na<sub>2</sub>MoO<sub>4</sub>·2H<sub>2</sub>O and C<sub>2</sub>H<sub>5</sub>NS. In order to distinguish between these samples, they were labeled as BiVO<sub>4</sub>@MoS<sub>2</sub> ( $x$  wt%) ( $x=2, 5, 10$  and  $20$ ), respectively. For comparison, pure MoS<sub>2</sub> nanosheets were synthesized under the same conditions without adding BiVO<sub>4</sub>.

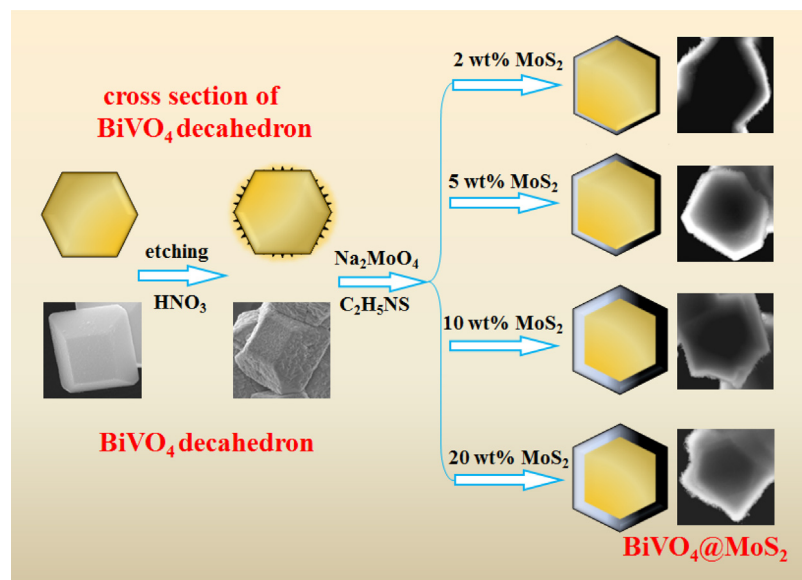


**Fig. 1.** Schematic of the synthesis of p–n heterojunction photocatalyst  $\text{BiVO}_4@\text{MoS}_2$ .

#### 2.4. Photoreaction procedures

The photocatalytic activities of as-synthesized samples were systematically investigated by the photocatalytic reduction of  $\text{Cr}^{6+}$  and photocatalytic oxidation of CV under visible-light irradiation. Visible-light was generated by using 500 W Xe lamp irradiation with a 420 nm cut-off filter to remove light of  $\lambda < 420 \text{ nm}$ . The amount of photocatalyst used was 0.4 g/L, the initial concentrations of  $\text{Cr}^{6+}$  and CV are 15 mg/L (which was based on Cr in a dilute  $\text{K}_2\text{Cr}_2\text{O}_7$  solution) and 25 mg/L, respectively. Prior to irradiation, the suspensions including 50 mL  $\text{Cr}^{6+}$  (or CV) solution and 0.02 g as-prepared sample were magnetically stirred for 60 min to reach adsorption–desorption equilibrium in the dark. After illumination, the samples (volume of each is 3 mL) were taken from the reaction suspension, centrifuged at 8000 rpm for 10 min and filtered through a 0.22  $\mu\text{m}$  Millipore filter to remove the particles. The filtrate was subsequently analyzed by UV–vis spectroscopy. To ensure the reproducibility of the results, duplicate runs were performed for each condition for averaging the results.

#### 2.5. Analytical methods

The concentration of  $\text{Cr}^{6+}$  in solution was determined by UV–vis spectroscopy using diphenylcarbazide reagent as a developer. The concentration of CV in solution was determined by UV–vis spectroscopy.

The photoreduction efficiency of  $\text{Cr}^{6+}$  and the photooxidation efficiency of CV were calculated from the following expression:

$$\eta = \frac{(C_0 - C_t)}{C_0} \times 100\%$$

where  $\eta$  is the photocatalytic efficiency;  $C_0$  is the initial concentration of reactant;  $C_t$  is the concentration of reactant after illumination time  $t$ .

The photocatalytic oxidation products of CV were identified by gas chromatography–mass spectrometer (GC–MS). The analytical methods have been reported by our group [31]. Prior to GC–MS analysis, the CV reaction solutions were extracted with 5 mL of dichloromethane for three times. The combined extracted solution was dehydrated using anhydrous sodium sulfate and concentrated to 1 mL by rotary evaporation ( $50^\circ\text{C}$ ), then the solvent was blown

away by the gentle nitrogen. In order to methylate the reaction byproducts, 0.2 mL of BSTFA/TMCS was added into the vial and mixed with the residue at  $50^\circ\text{C}$  for 30 min. Degradation products were analyzed by GC–MS analysis using a Thermo Finnigan gas chromatograph interfaced with a Polaris Q ion trap mass spectrometer and with a DB-5 GC column ( $30 \text{ m} \times 0.25 \text{ mm i.d.}, 0.25 \mu\text{m}$ , Agilent). The oven temperature program was set from  $60^\circ\text{C}$  (2 min) to  $110^\circ\text{C}$  at  $7 \text{ min}^{-1}$  and from  $110$  to  $300^\circ\text{C}$  (8 min) at  $13^\circ\text{C min}^{-1}$ . The MS was operated in positive electron impact (EI) ionization mode with electron energy of 70 eV. The injector temperature was  $240^\circ\text{C}$ . Helium was used as carrier gas.

#### 2.6. Characterization

The crystallinity of the sample was determined by X-ray diffraction (XRD) at room temperature using an X’Pert-ProMPD (Holand) D/max- $\gamma\text{A}$  X-ray diffractometer. X-ray photo-electron spectroscopy (XPS) was performed to identify surface chemical composition and chemical states of the catalysts on a PHI5000 Versa Probe electron spectrometer (ULVAC-PHI, Japan). The field emission scanning electron microscopy (FESEM) images were taken on a FEI-quanta 200F scanning electron microscope with an acceleration voltage of 20 kV. Transmission electron micrograph (TEM) and High resolution transmission electron microscopy (HRTEM) were taken on a FEI-Tecnai F20 (200 kV) transmission electron microscope (FEI). Fluorescence emission spectra were recorded on a FluoroMax 4 type fluorescence spectrophotometer with an excitation wavelength at 425 nm. The lifetimes of the charge carriers were measured using a nanosecond Hydrogen flash lamp as the excitation source and a time correlated single photon counting (TCSPC) technique. The samples were excited at 320 nm and the lifetime was monitored for 550 nm emission. UV–vis absorption spectra were carried out using a Lambda 750 (PerkinElmer) spectrophotometer at a wavelength range of 200–800 nm. The photocurrent experiments were performed using an electrochemical station (CHI660D, Shanghai Chenhua Ltd., China) in a conventional three-electrode configuration. The electrolyte was 0.01 M  $\text{Na}_2\text{SO}_4$  aqueous solution. The specific surface area was determined by  $\text{N}_2$  adsorption (the BET method) at  $150^\circ\text{C}$  using a Quantachrome NOVA 2000e adsorption instrument.

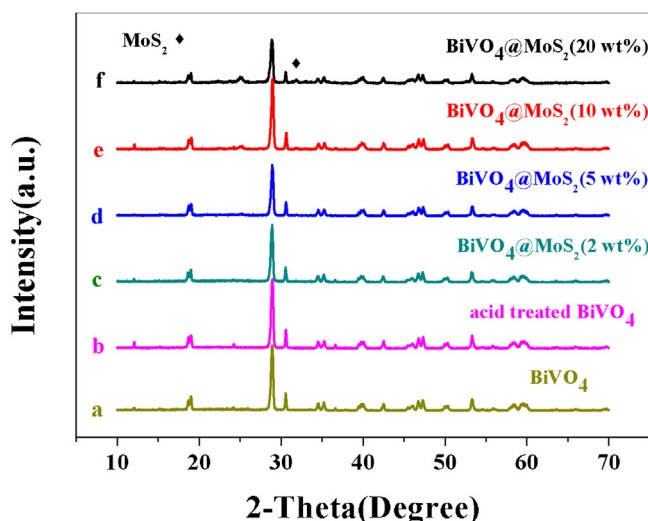


**Fig. 2.** XRD patterns of the as-prepared samples (♦ mark shows the presence of MoS<sub>2</sub>).

### 3. Results and discussion

XRD was used to determine the crystallographic structures and phase purities of the as-prepared BiVO<sub>4</sub> and BiVO<sub>4</sub>@MoS<sub>2</sub> photocatalyst. Curves a and b in Fig. 2 are XRD patterns of the BiVO<sub>4</sub> before and after the acid treatment, respectively. All the diffraction peaks can be indexed to the body-centered monoclinic phase of BiVO<sub>4</sub> [JCPDS: 14-0666]. Comparison of curve a and b clearly indicates that there is no crystal phase change in the two samples before and after acid treatment. Curve c–f in Fig. 2 shows the XRD patterns of p–n heterojunction photocatalyst BiVO<sub>4</sub>@MoS<sub>2</sub> with different MoS<sub>2</sub> content. From Fig. 2, it is clear that when the loading amount of MoS<sub>2</sub> is lower than 10 wt%, the diffraction peaks of MoS<sub>2</sub> cannot be found in XRD patterns. It is proposed that MoS<sub>2</sub> may be uniformly coated on the sample, and the amount of MoS<sub>2</sub> is so small that the equipment does not detect its existence. When the loading amount of MoS<sub>2</sub> is 20 wt%, the weak diffraction peaks located at 33°, which corresponds to the (1 0 0) plane of MoS<sub>2</sub>, can be found in XRD patterns (curve f). In order to further verify the existence of MoS<sub>2</sub>, the BiVO<sub>4</sub>@MoS<sub>2</sub> was further examined by XPS, FESEM and TEM analyses.

The surface chemical composition and chemical states of MoS<sub>2</sub> and BiVO<sub>4</sub>@MoS<sub>2</sub> were analyzed by XPS. In Fig. S1a, the survey scan XPS spectra of BiVO<sub>4</sub>@MoS<sub>2</sub> suggest that the composite contains C, Mo, S, Bi, V, and O, which is consistent with chemical composition of the photocatalyst. It is proposed that the C 1s peak at around 284.6 eV can be assigned to the signal from carbon contained in the apparatus and is used for calibration. Fig. 3a and b show the high-resolution XPS spectra of Mo 3d and S 2p, respectively. For the pure MoS<sub>2</sub>, the binding characteristic orbital of S 2p<sub>1/2</sub>, S 2p<sub>3/2</sub>, Mo 3d<sub>3/2</sub> and Mo 3d<sub>5/2</sub> peaks are observed with peak locations at 163.3, 162.3, 232.5 and 229.3 eV, respectively, which are all consistent with the reported values for MoS<sub>2</sub> crystal [32]. After MoS<sub>2</sub> nanosheets coating onto the BiVO<sub>4</sub>, S 2p<sub>1/2</sub>, S 2p<sub>3/2</sub>, Mo 3d<sub>3/2</sub> and Mo 3d<sub>5/2</sub> peaks shift to 162.8, 161.8, 232.1 and 228.9 eV, respectively. It is clear that the binding energies of BiVO<sub>4</sub>@MoS<sub>2</sub> shift to the lower energy compared with pure MoS<sub>2</sub>, which may be attributed to the heterostructure effect between MoS<sub>2</sub> and BiVO<sub>4</sub>. As shown in Fig. S1b–c, the characteristic peaks of the Bi 4f<sub>7/2</sub>, Bi 4f<sub>5/2</sub> and the V 2p<sub>3/2</sub>, V 2p<sub>1/2</sub> of the BiVO<sub>4</sub>@MoS<sub>2</sub> are observed at approximately 158.8, 164.1 and 517.0, 524.6 eV, respectively, which are closely consistent with the Bi<sup>3+</sup> and V<sup>5+</sup> peaks in monoclinic scheelite BiVO<sub>4</sub> [33]. From high-resolution scanning XPS spectra of O 1s

in Fig. S1d, the O 1s peaks can be further deconvoluted three bands (530.4, 532.2 and 534.0 eV), implying the presence of three forms of oxygen on the sample surface. The peak at 530.4 eV is mainly assigned to the O<sup>2-</sup> anion [34]. The peak at 532.2 eV attributes to oxygen in the sample surface adsorption of (-OH). The peak at 534.0 eV can be ascribed to the adsorbed water molecules on the surface [35–37]. It is just because so much adsorption oxygen atoms exist on the sample surface that they become captives of photogenerated electron–hole pairs directly or indirectly, which further inhibits the photogenerated electron–hole recombination, prolongs the lifetime of the photogenerated carriers, increases the quantum efficiency and hence effectively improves the photocatalytic activity of the sample.

The morphologies of the as-synthesized BiVO<sub>4</sub> and BiVO<sub>4</sub>@MoS<sub>2</sub> photocatalyst were investigated by FESEM. The morphologies of the synthesized BiVO<sub>4</sub> are shown in Fig. 4a and b. The as-prepared BiVO<sub>4</sub> powder shows a smooth surface, regular decahedron shape with a size of 1–2 μm. After the nitric acid treatment, the surface of BiVO<sub>4</sub> became rough and corroded compared to the pure BiVO<sub>4</sub> (Fig. S2a in Supporting information (SI)). The rough surface with abundant defects can act as nucleation sites for the growth of MoS<sub>2</sub> nanosheets. Without the acid treatment, the MoS<sub>2</sub> nanosheets are not uniformly coated on the surface of BiVO<sub>4</sub>, only a small amount of MoS<sub>2</sub> nanosheets are randomly grown on the smooth surface of the untreated BiVO<sub>4</sub> (Fig. S2b in SI). These results show that acid treatment may play a key role in the synthesis of BiVO<sub>4</sub>@MoS<sub>2</sub> with core–shell structure. The BiVO<sub>4</sub>@MoS<sub>2</sub> heterojunctions with the different loading amounts of MoS<sub>2</sub> (from 2 to 20 wt%) are shown in Fig. 4c–g. The uniform coating of MoS<sub>2</sub> thin layers around the whole surface of BiVO<sub>4</sub> crystals is clearly evidenced. Moreover, the relatively low-magnification and high-magnification images of BiVO<sub>4</sub>@MoS<sub>2</sub> (10 wt%) are shown in Fig. 4e and f, respectively. It is clear that the thin MoS<sub>2</sub> nanosheets are uniformly deposited on the surface of BiVO<sub>4</sub> to form BiVO<sub>4</sub>@MoS<sub>2</sub> core–shell composite.

Furthermore, the detailed morphology and microstructure of the pure MoS<sub>2</sub> and BiVO<sub>4</sub>@MoS<sub>2</sub> was examined by TEM and HRTEM. Fig. 5a shows that the pure MoS<sub>2</sub> nanosheets are clustered to form MoS<sub>2</sub> microspheres with a diameter of 500–700 nm when it was prepared by the same hydrothermal method without the addition of BiVO<sub>4</sub>. The TEM images of BiVO<sub>4</sub>@MoS<sub>2</sub> are demonstrated in Fig. 5b–e, the contrast between dark center and gray edge with the thickness of about 80–300 nm is clearly observed, indicating the formation of core–shell structure of the sample. Importantly, the thickness of the shell can be adjusted in the preparation process by changing the loading amount of MoS<sub>2</sub>. The increase loading amount of MoS<sub>2</sub> results in the formation of thicker MoS<sub>2</sub> shell on BiVO<sub>4</sub> surfaces. As the loading amount of MoS<sub>2</sub> are 2, 5, 10, and 20 wt%, the thickness of the corresponding MoS<sub>2</sub> shell on the core BiVO<sub>4</sub> particles are about 80, 150, 300 and 300 nm, respectively. The result illustrates that when the loading amount of MoS<sub>2</sub> is beyond 10 wt%, the thickness does not significantly increase. From the HRTEM image in Fig. 5f, the interplanar distances are determined to be 0.27 and 0.26 nm, which are in accordance with the D-spacing of the (1 0 0) crystal plane of MoS<sub>2</sub> and (2 0 0) crystal plane of BiVO<sub>4</sub>, respectively [38].

Fig. 6a and b shows SEM-EDS elemental mapping of BiVO<sub>4</sub> and BiVO<sub>4</sub>@MoS<sub>2</sub>, respectively. The 2D-projected elemental mapping of BiVO<sub>4</sub> sample discloses in Fig. 6a, demonstrates the distribution of Bi, V, and O elements throughout the BiVO<sub>4</sub> sample. For BiVO<sub>4</sub>@MoS<sub>2</sub>, apart from these elements, the element of Mo/S is found (Fig. 6b) also. In addition, EDS analysis confirms the elemental composition of BiVO<sub>4</sub>@MoS<sub>2</sub>, as shown in Fig. 4h, which also reveals the coexistence of Bi, V, O, Mo and S elements. Based on the above characterization results, it can be verified that BiVO<sub>4</sub>@MoS<sub>2</sub> photocatalysts have been successfully prepared.

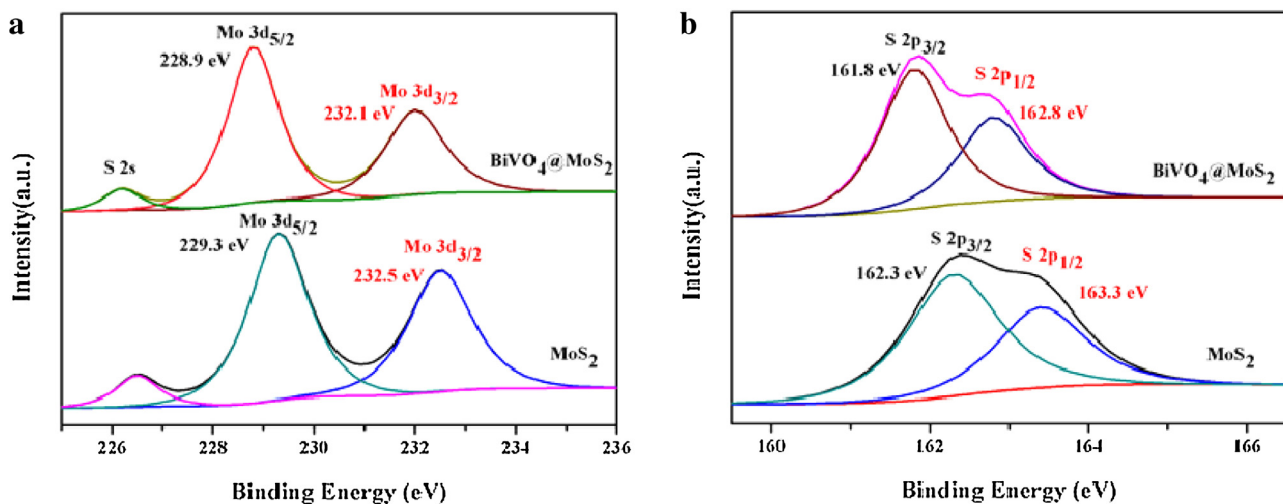


**Fig. 3.** (a) XPS spectra of Mo 3d peaks of MoS<sub>2</sub> and BiVO<sub>4</sub>@MoS<sub>2</sub>, (b) S 2p peaks of MoS<sub>2</sub> and BiVO<sub>4</sub>@MoS<sub>2</sub>.

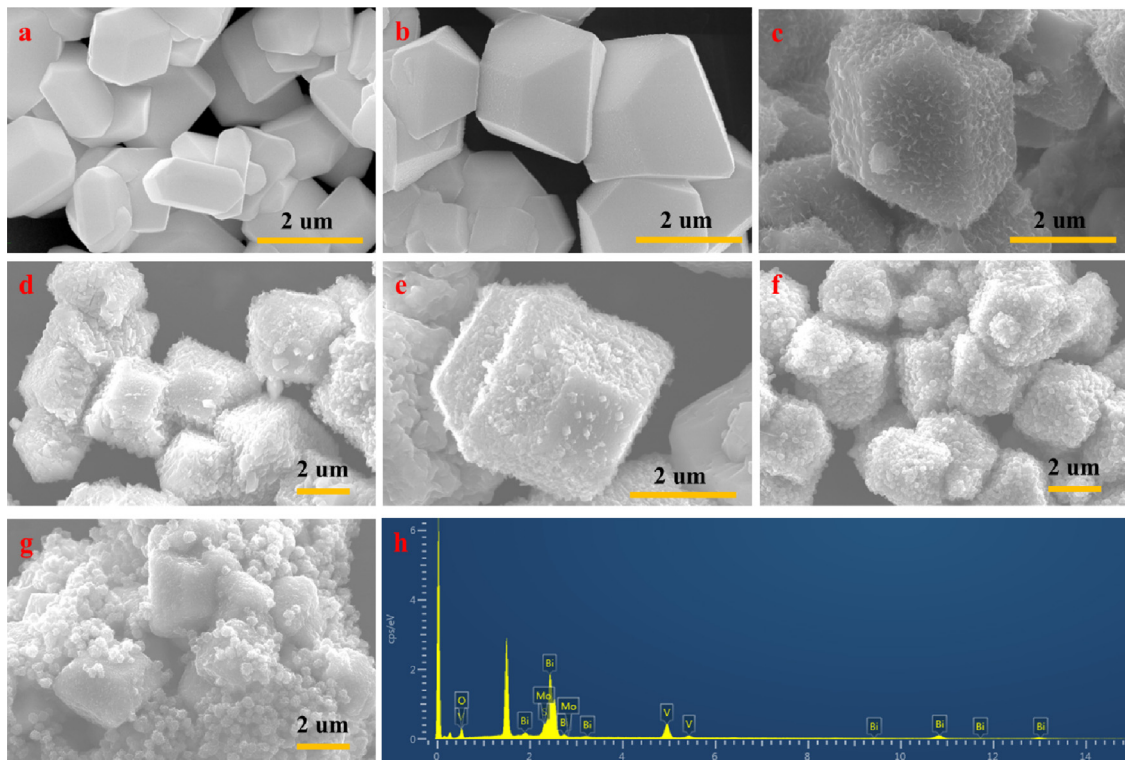


**Fig. 4.** (a) Low magnification FESEM image of BiVO<sub>4</sub>, (b) high magnification FESEM image of BiVO<sub>4</sub>, (c) the FESEM images of BiVO<sub>4</sub>@MoS<sub>2</sub> (2 wt%), (d) the FESEM image of BiVO<sub>4</sub>@MoS<sub>2</sub> (5 wt%), (e) low magnification FESEM image of BiVO<sub>4</sub>@MoS<sub>2</sub> (10 wt%), (f) high magnification FESEM image of BiVO<sub>4</sub>@MoS<sub>2</sub> (10 wt%), (g) the FESEM image of BiVO<sub>4</sub>@MoS<sub>2</sub> (20 wt%), (h) EDS pattern of BiVO<sub>4</sub>@MoS<sub>2</sub>.

The photoluminescence (PL) emission spectra of the samples were performed to study the separation rate of electron–hole pairs, which could greatly affect the catalytic activity. Fig. 7 presents the PL spectra of BiVO<sub>4</sub> and BiVO<sub>4</sub>@MoS<sub>2</sub> with an excitation wavelength of 425 nm. It can be seen from the figure that the pure BiVO<sub>4</sub> has a wide emission peak centered at around 550 nm, which is considered to result from the recombination of the hole formed in the O 2p band and the electron in the V 3d band [39]. It is clear that the relative intensity of the emission spectra of BiVO<sub>4</sub> is the greatest, which means that electrons and holes of BiVO<sub>4</sub> are easy to recombine. The relative intensity of the BiVO<sub>4</sub>@MoS<sub>2</sub> (2.0, 5.0, 10, 20 wt%) is lower than that of BiVO<sub>4</sub>, indicating that MoS<sub>2</sub> coated could suppress the recombination of electrons and holes due to the formation

of heterojunction structure. Interestingly, the intensities of PL spectra correlate with the MoS<sub>2</sub> content. The intensities of PL spectra for BiVO<sub>4</sub>@MoS<sub>2</sub> decrease with increasing of MoS<sub>2</sub> content, and reached minimum at MoS<sub>2</sub> content of 10 wt%. Further increasing the MoS<sub>2</sub> content to 20 wt%, the intensities of PL spectra do not decrease, which shows that 10 wt% depositing quantity of MoS<sub>2</sub> can effectively restrain the recombination of electrons and holes. It is proposed that only the BiVO<sub>4</sub> deposited with suitable amount of MoS<sub>2</sub>, both BiVO<sub>4</sub> and MoS<sub>2</sub> can efficiently form the p-n heterojunction photocatalyst, therefore, too high and too low MoS<sub>2</sub> contents are not helpful to form BiVO<sub>4</sub>@MoS<sub>2</sub> core–shell structure and to facilitate the charge transfer. These analyses also coincide with the photocatalytic activity of the photocatalysts.

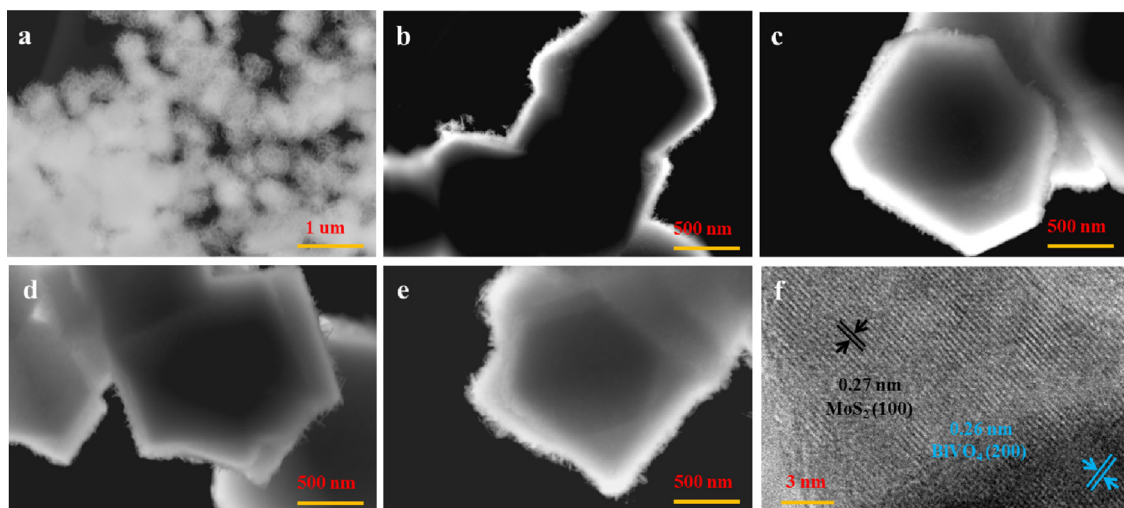


**Fig. 5.** (a) TEM image of MoS<sub>2</sub>, (b) TEM image of BiVO<sub>4</sub>@MoS<sub>2</sub> (2 wt%), (c) TEM image of BiVO<sub>4</sub>@MoS<sub>2</sub> (5 wt%), (d) TEM image of BiVO<sub>4</sub>@MoS<sub>2</sub> (10 wt%), (e) TEM image of BiVO<sub>4</sub>@MoS<sub>2</sub> (20 wt%), and (f) HRTEM image of BiVO<sub>4</sub>@MoS<sub>2</sub> (10 wt%).

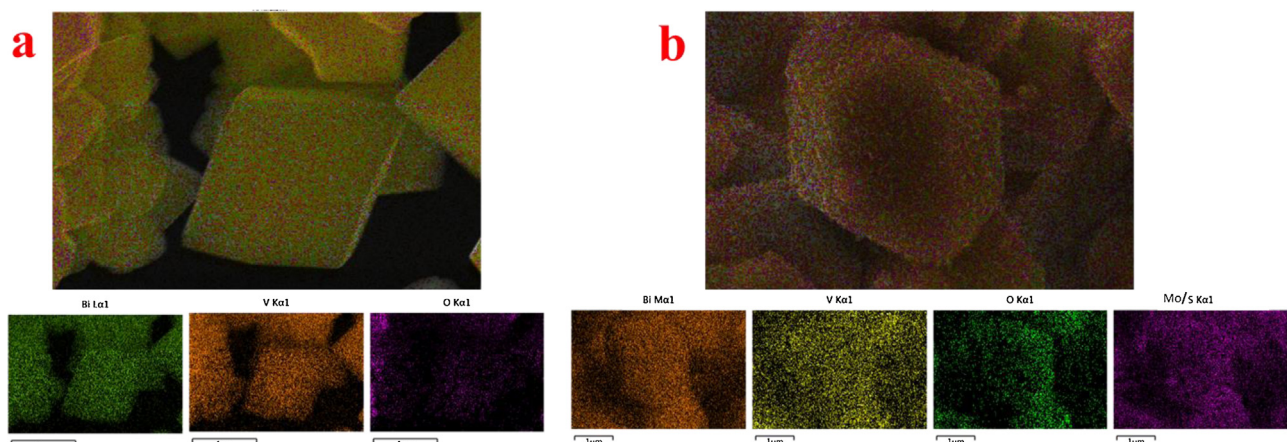


**Fig. 6.** SEM-EDS elemental mapping of (a) BiVO<sub>4</sub> and (b) BiVO<sub>4</sub>@MoS<sub>2</sub>.

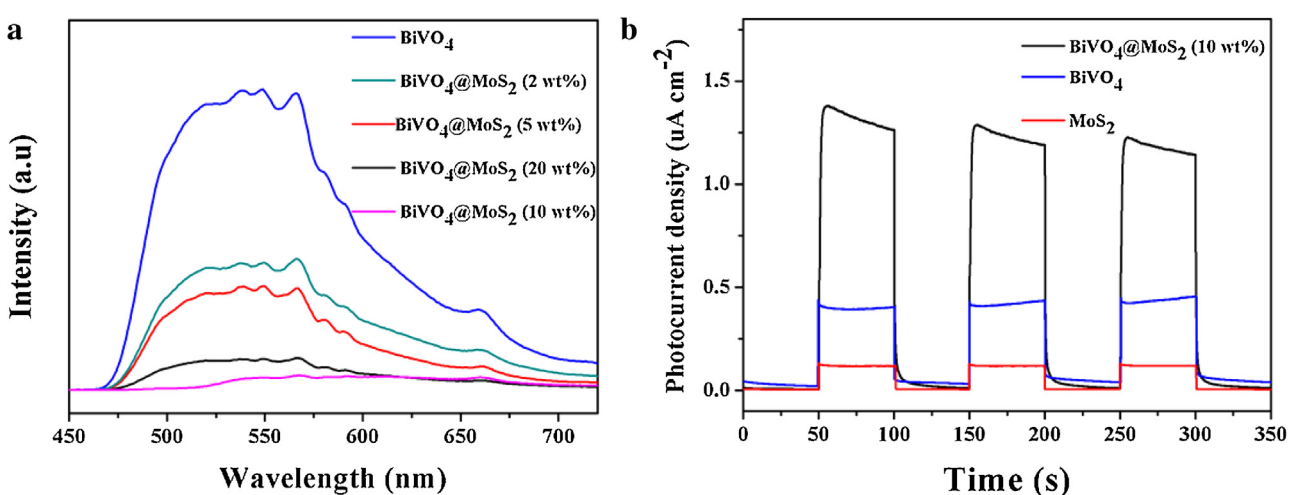


**Fig. 7.** (a) PL spectra of as-prepared BiVO<sub>4</sub> and BiVO<sub>4</sub>@MoS<sub>2</sub>, (b) photocurrent of BiVO<sub>4</sub>, MoS<sub>2</sub> and BiVO<sub>4</sub>@MoS<sub>2</sub>.

Photocurrent measurements were also carried out to investigate the photoresponses of the BiVO<sub>4</sub>, MoS<sub>2</sub> and BiVO<sub>4</sub>@MoS<sub>2</sub>. The higher photocurrent value means more efficient separation of photogenerated electron-hole pairs. As shown in Fig. 7b, the

BiVO<sub>4</sub>@MoS<sub>2</sub> heterojunction displays much stronger photocurrent intensity than BiVO<sub>4</sub> and MoS<sub>2</sub> nanosheets, illustrating strong ability of producing charge carriers and favorably separated electrons.

In order to further confirm the efficient charge separation between BiVO<sub>4</sub> and MoS<sub>2</sub>, time-resolved fluorescence emission decay spectra were measured. The average lifetimes of the carriers ( $\tau_{\text{avg}}$ ) were determined to be 1.39 ns and 2.88 ns for BiVO<sub>4</sub> and BiVO<sub>4</sub>@MoS<sub>2</sub> respectively (Fig. S3a and b). The increased lifetime of the charge carriers in the BiVO<sub>4</sub>@MoS<sub>2</sub> indicates that MoS<sub>2</sub> shell plays a role in increasing the lifetime of the photogenerated charges.

Thus, the above results of PL spectra, photocurrent measurements and time-resolved fluorescence emission decay spectra further prove that the BiVO<sub>4</sub>@MoS<sub>2</sub> heterojunction possesses a relatively lower electron–hole recombination rate and a comparatively higher charge separation efficiency under visible-light.

UV-vis absorption spectra of BiVO<sub>4</sub>, MoS<sub>2</sub>, and BiVO<sub>4</sub>@MoS<sub>2</sub> are illustrated in Fig. 8a. The bare MoS<sub>2</sub> nanosheets show significant absorption both in the ultraviolet and visible regions. For the pure BiVO<sub>4</sub>, a strong absorption at wavelength shorter than around 500 nm attribute to the intrinsic band gap absorption. After depositing MoS<sub>2</sub> nanosheets on the surface of BiVO<sub>4</sub>, the optical absorption of the composites in the visible region increases compared with the pure BiVO<sub>4</sub>, indicating the composite should possess better visible-light photocatalytic performance. In addition, the band gap energy ( $E_g$ ) of BiVO<sub>4</sub> and MoS<sub>2</sub> samples was calculated by:  $(\alpha h\nu)^n = A(h\nu - E_g)$ , where  $\alpha$ ,  $h$ ,  $\nu$ ,  $E_g$ , and  $A$  are the absorption coefficient, Planck's constant, light frequency, band gap and a constant, respectively. The index  $n$  depends on the electronic transition of the semiconductor,  $n=2$  for direct-gap semiconductor and  $n=0.5$  for indirect-gap semiconductor. For MoS<sub>2</sub> and BiVO<sub>4</sub>,  $n$  is 2. The corresponding Kubelka–Munk transformed reflectance spectra is shown in Fig. 8 where the band gap energy can be estimated from the intercept of the tangent to the plot of  $(\alpha h\nu)^2$  vs. radiation energy ( $h\nu$ ). The obtained band gap energy for BiVO<sub>4</sub> is 2.50 eV, which is consistent with the previous report [40]. Whereas the band gap energy of MoS<sub>2</sub> is about 1.62 eV, the large blue shift of band gap energy from the MoS<sub>2</sub> nanosheets compared to the bulk MoS<sub>2</sub> with the band gap energy of 1.23 eV [41], can be assigned to the strong quantum confinement effect of the thin nanosheets, which also makes the MoS<sub>2</sub> nanosheets as an effective visible-light photocatalyst [42]. As for the BiVO<sub>4</sub>@MoS<sub>2</sub> composite materials, the values of band gap energy are 2.19, 2.09 and 1.90 eV for the BiVO<sub>4</sub>@MoS<sub>2</sub> (2 wt%), BiVO<sub>4</sub>@MoS<sub>2</sub> (5 wt%), and BiVO<sub>4</sub>@MoS<sub>2</sub> (10 wt%), respectively.

The photocatalytic activities of BiVO<sub>4</sub>, MoS<sub>2</sub>, and BiVO<sub>4</sub>@MoS<sub>2</sub> were investigated in terms of the photocatalytic reduction of Cr<sup>6+</sup> and oxidation of CV under visible-light irradiation. A dark adsorption experiment was performed for 60 min prior to the visible-light irradiation to achieve an equilibrium adsorption state. It is clear that the BiVO<sub>4</sub>@MoS<sub>2</sub> displayed distinctly higher adsorptive ability than the bare BiVO<sub>4</sub>. This could be attributed to the deposition of MoS<sub>2</sub> nanosheets with the large specific surface area in the former system. Evidently, after MoS<sub>2</sub> nanosheets coated on the surface of BiVO<sub>4</sub>, the specific surface area of the BiVO<sub>4</sub>@MoS<sub>2</sub> with 10 wt% of MoS<sub>2</sub> (26.9 m<sup>2</sup>/g) is higher than that of the bare BiVO<sub>4</sub> (6.8 m<sup>2</sup>/g).

Fig. 9a presents the photocatalytic reduction of Cr<sup>6+</sup> over the samples. After 90 min of visible-light irradiation, 5.9% of Cr<sup>6+</sup> reduction was achieved over MoS<sub>2</sub>, and the BiVO<sub>4</sub> displayed a relatively high photocatalytic activity with Cr<sup>6+</sup> reduction of 12.1%. All the BiVO<sub>4</sub>@MoS<sub>2</sub> manifested remarkably higher photocatalytic reduction activities than those of pure BiVO<sub>4</sub> and MoS<sub>2</sub>. Moreover, the content of MoS<sub>2</sub> nanosheets has a significant influence on the photocatalytic reduction activity of BiVO<sub>4</sub>@MoS<sub>2</sub>. It can be seen that the photoreduction activity of BiVO<sub>4</sub>@MoS<sub>2</sub> increases remarkably with increasing the amount of MoS<sub>2</sub> up to 10 wt%, indicating that the optimum amount of MoS<sub>2</sub> is 10 wt%. The BiVO<sub>4</sub>@MoS<sub>2</sub> (10 wt%) sample exhibits the highest photoreduction activity with 76.5% of Cr<sup>6+</sup> reduced. While the photoreduction activity of BiVO<sub>4</sub>@MoS<sub>2</sub> (20 wt%) decreases as the amount of MoS<sub>2</sub> is higher than optimal

amount. Obviously, there is an optimal depositing amount of MoS<sub>2</sub> nanosheets on the BiVO<sub>4</sub> in terms of Cr<sup>6+</sup> photocatalytic reduction efficiency. Too low and too high MoS<sub>2</sub> contents do not facilitate to enhance the photoreduction activity of BiVO<sub>4</sub>@MoS<sub>2</sub>. It is proposed that when the amount of MoS<sub>2</sub> is lower than its optimum amount of depositing, the trapping sites of carriers increase with the increase of the MoS<sub>2</sub> amount, which prolongs the lifetime of carriers, thus improving the photocatalytic activity. In addition, BiVO<sub>4</sub> coated with a proper amount of MoS<sub>2</sub> forms a p–n heterojunction photocatalyst through hydrothermal method, so that the photocatalytic performance increases. However, when the amount of MoS<sub>2</sub> is higher than its optimum amount of depositing, excessive MoS<sub>2</sub> (for example, 20 wt%) may be clustered and do not effectively form the p–n heterojunction photocatalyst under this condition, which is confirmed by the SEM result (Fig. 4g). Furthermore, excessive loading of MoS<sub>2</sub> may block photogenerated electrons transfer and reduce active site exposure due to high overlapping each other.

Additionally, the physical mixture of BiVO<sub>4</sub> and MoS<sub>2</sub> nanosheets (BiVO<sub>4</sub> + MoS<sub>2</sub>, with a weight ratio of 9:1), exhibits a appreciably lower photocatalytic activity than the in-situ synthesized BiVO<sub>4</sub>@MoS<sub>2</sub> by hydrothermal method, which can be attributed to the poor interfacial contact between MoS<sub>2</sub> and BiVO<sub>4</sub> for the physical mixture of BiVO<sub>4</sub> + MoS<sub>2</sub>, implying the importance of the core–shell heterojunction with intimate interfacial contact in the improvement of photocatalytic performance. Therefore, in the BiVO<sub>4</sub>@MoS<sub>2</sub> heterojunction, the intimate interfacial contact between the two components provides the efficient charge separation to suppress the electron–hole recombination, which greatly enhances the performance in the Cr<sup>6+</sup> photocatalytic reduction.

The stability and recyclability of the catalysts are important issues in the practice application. We have further studied the stability and reusability of BiVO<sub>4</sub>@MoS<sub>2</sub> by collecting and reusing the same photocatalyst for 5 cycles (Fig. 9b). As shown in Fig. 9b, the photocatalyst demonstrated adequate stability and reusability. Only insignificant loss in photocatalytic activity is observed, which might be partly caused by incomplete collection of the photocatalyst during each step.

The photooxidation activities of samples were also evaluated by the photocatalytic oxidation of CV solution under visible-light irradiation, as shown in Fig. 9c. The results are similar to the photocatalytic reduction of Cr<sup>6+</sup>. The BiVO<sub>4</sub>@MoS<sub>2</sub> (10 wt%) sample exhibits the highest photooxidation activity with the photooxidation efficiency of 69.2% after 60 min of visible-light irradiation. The stability of the BiVO<sub>4</sub>@MoS<sub>2</sub> (10 wt%) during the photocatalytic oxidation of CV was also investigated, as shown in Fig. 9d, the sample exhibited adequate stability.

Zhou et al. reported that the sample TiO<sub>2</sub>@MoS<sub>2</sub> heterostructure took about 20 min to completely degrade Rhodamine B (10 mL, 15 mg/L) [28]. The removal of Cr<sup>6+</sup> (20 mL, 10 mg/L) by BiVO<sub>4</sub>/Bi<sub>2</sub>S<sub>3</sub> heterostructure was 91.2% within 60 min [25]. Compared with these studies, the photocatalytic activities of BiVO<sub>4</sub>@MoS<sub>2</sub> were rather perfect and effective.

It is generally acknowledged that photo-excited electrons play a key role in the photocatalytic reduction reaction, while there are a lot of main reactive oxygen species involved in the photocatalytic oxidation process, such as •O<sub>2</sub><sup>-</sup>, h<sup>+</sup> and •OH [43–45]. In order to detect the effect of these reactive species on the photocatalytic oxidation of CV, as an •O<sub>2</sub><sup>-</sup> scavenger, benzoquinone (BQ) was added to the reaction system, and ammonium oxalate (AO) was introduced as the scavenger of h<sup>+</sup>. Isopropanol (IPA) was adopted to quench •OH. The comparative experiment with no quencher was also carried out under otherwise identical conditions. As a result of quenching, photocatalytic oxidation would be partly suppressed and the value of photooxidation efficiency was lowered. The lower the value of photooxidation efficiency is caused by scavengers, the more important role the corresponding oxidizing species plays in

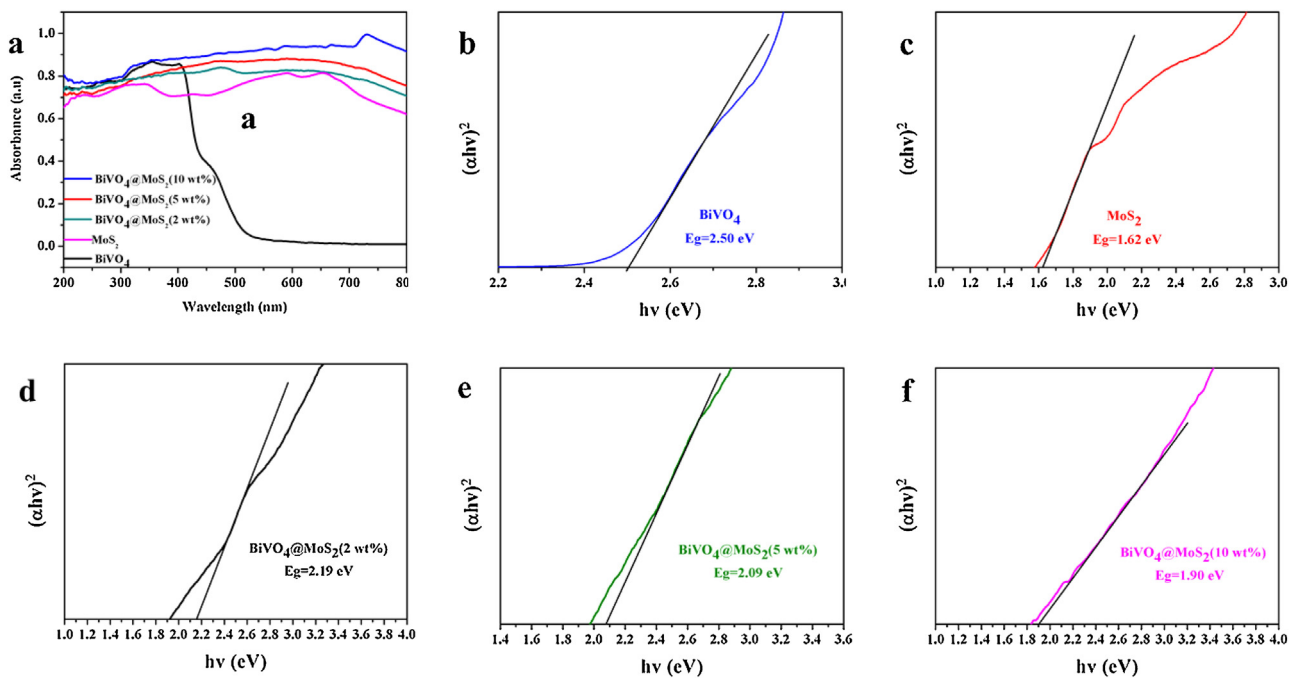


**Fig. 8.** (a) UV-vis absorption spectra of as-prepared BiVO<sub>4</sub>, MoS<sub>2</sub> and BiVO<sub>4</sub>@MoS<sub>2</sub>, (b-f) the plot of  $(\alpha h\nu)^2$  vs. energy  $h\nu$  and band gap energy of the as-prepared samples.

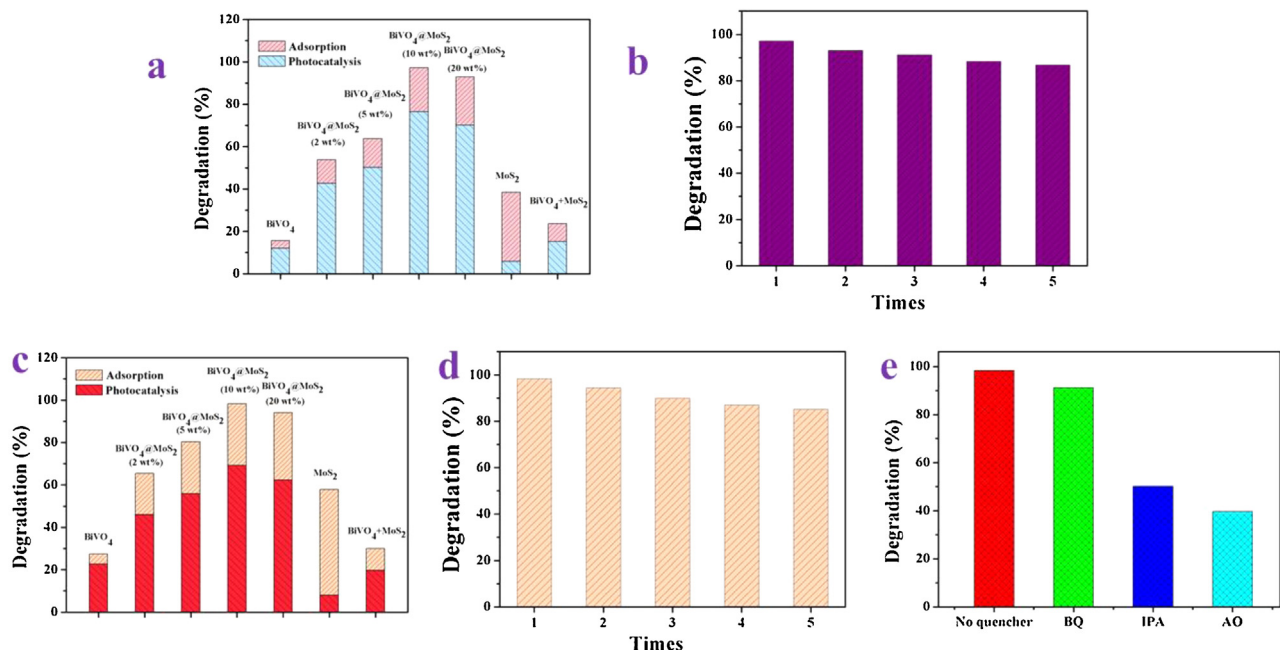


**Fig. 9.** (a) Photocatalytic reduction activities of as-prepared photocatalysts, (b) 5 recycling runs of BiVO<sub>4</sub>@MoS<sub>2</sub> for Cr<sup>6+</sup> reduction, (c) photocatalytic oxidation activities of as-prepared photocatalysts, (d) 5 recycling runs of BiVO<sub>4</sub>@MoS<sub>2</sub> for CV oxidation degradation, (e) the effect of different quenchers on the photocatalytic oxidation of CV.

the photocatalytic oxidation. From Fig. 9e, BQ shows little effect on the CV degradation, which indicates that  $\bullet\text{O}_2^-$  is not the main reactive species in the photocatalytic oxidation process. However, upon the addition of AO and IPA, the values of photooxidation efficiency both decreased seriously, suggesting that  $\bullet\text{OH}$  and  $\text{h}^+$  are the main reactive species in the photocatalytic oxidation process.

The intermediates and products formed in the photocatalytic oxidation degradation of CV were identified by the analysis of mass spectra obtained from GC-MS applications. There were 12 intermediates, mostly substituted benzenes and small molecular weight alcohols, identified from the photocatalytic oxidation pro-

cess. Table 1 lists main fragments ( $m/z$ ) and retention time (min) obtained for 12 intermediate products. These degradation products indicate extensive cleavage of the CV chromophore structure. As suggested from the result of reactive species experiment,  $\bullet\text{OH}$  and  $\text{h}^+$  are the main reactive species in the photocatalytic oxidation of CV. It is known that  $\bullet\text{OH}$  and  $\text{h}^+$  are nonselective radicals, hence more reactive sites are available for these radicals to attack, which is consistent with a number of CV degradation products.

In photocatalytic systems, p-n heterojunction is an interesting structure which could accelerate the efficient separation of electron-hole pairs [46–49]. It is well known that MoS<sub>2</sub> is a p-type

**Table 1**  
Identification of the intermediates of CV by GC-MS.

Product	Retention time (min)	m/z	Molecular structure
1	15.78	210	
2	6.19	152	
3	7.15	110	
4	8.38	136	
5	9.20	124	
6	14.28	206	
7	11.87	123	
8	10.01	107	
9	11.80	116	
10	14.94	146	
11	9.75	90	
12	9.69	46	

semiconductor, and BiVO<sub>4</sub> is an n-type semiconductor. Theoretically, when the p-type MoS<sub>2</sub> and the n-type BiVO<sub>4</sub> form p-n heterojunction structure, an inner electric field is formed simultaneously with a negatively charged portion at the interface of the p-type MoS<sub>2</sub> region and with a positively charged portion at the interface of the n-type BiVO<sub>4</sub> region. Under the inner electric field, the holes flow into the negative field while the electrons move to

the positive field. Thus, the photogenerated electrons and holes are separated efficiently, and the photocatalytic activity is enhanced.

In addition, the photocatalytic property of the photocatalyst is related to its band structure. The band edge positions of both the conduction band and the valence band can be determined with a simple approach [50]. The conduction band edge ( $E_{CB}$ ) of a semiconductor at the point of zero charge (pH<sub>ZPC</sub>) can be predicted by the following equation:

$$E_{CB} = X - E^e - 0.5E_g$$

where  $X$  is the absolute electronegativity of the semiconductor,  $E^e$  is the energy of free electrons on the hydrogen scale (4.5 eV),  $E_g$  is the band gap of the semiconductor which can be obtained from Fig. 3b and c, and the valence band edge ( $E_{VB}$ ) can be determined by  $E_{VB} = E_{CB} + E_g$ . Given the equation above, the  $E_{CB}$  values of BiVO<sub>4</sub> and MoS<sub>2</sub> are calculated to be 0.29 and 0.03 eV, respectively. Accordingly, the  $E_{VB}$  values of BiVO<sub>4</sub> and MoS<sub>2</sub> are estimated to be 2.79 and 1.65 eV, respectively. The calculated values are slightly more anodic than the measured values, but it does not affect the comparison of their relative positions.

Based on the band energy structure, both the conduction band (CB) and valence band (VB) positions of MoS<sub>2</sub> are higher than those of BiVO<sub>4</sub>. Under visible-light irradiation, the photogenerated electrons from the CB of MoS<sub>2</sub> are transferred to the CB of BiVO<sub>4</sub>, while the photogenerated holes from the VB of BiVO<sub>4</sub> are transferred to the VB of MoS<sub>2</sub>, which makes charge separation more efficient (Eqs. (1)–(4)). Thus, the enhancement of photocatalytic performance of the BiVO<sub>4</sub>@MoS<sub>2</sub> can be ascribed to inner electric field assisted charge transfer at the heterojunction interfaces between the components with matching band potentials, which consequently reduces the recombination of the photogenerated charge carriers greatly.

Moreover, the reduction potential of O<sub>2</sub>/•O<sub>2</sub><sup>-</sup> is –0.33 eV [51], the CB edge potential of BiVO<sub>4</sub> (0.29 eV) is not negative enough to reduce O<sub>2</sub> to •O<sub>2</sub><sup>-</sup> radicals. Therefore, the enriched electrons on the surface of BiVO<sub>4</sub> could not be trapped by molecular oxygen in solution to form •O<sub>2</sub><sup>-</sup>, which also make more electrons participate in the photocatalytic reduction of Cr<sup>6+</sup> as shown in Eq. (5), and hence enhance the photoreduction activity.

Furthermore, the VB potential of MoS<sub>2</sub> (1.65 eV) is not positive enough compared with the standard reduction potential of •OH/H<sub>2</sub>O (2.27 eV) or •OH/OH<sup>-</sup> (2.38 eV) [52], indicating that the most of h<sup>+</sup> on the surface of MoS<sub>2</sub> cannot oxidize H<sub>2</sub>O or OH<sup>-</sup> into •OH. Thus, theoretically, the photocatalytic oxidation degradation of CV could be mainly attributed to the direct reaction with h<sup>+</sup> (Eq. (6)). Fortunately, the VB potential of BiVO<sub>4</sub> is 2.79 eV, it is proposed that the partial h<sup>+</sup> from the BiVO<sub>4</sub> can oxidize H<sub>2</sub>O and OH<sup>-</sup> into •OH radicals (Eq. (7)–(9)). The experiment of the role of reactive species has also proved that h<sup>+</sup> and •OH radicals are the main reactive species in the photocatalytic oxidation of CV.



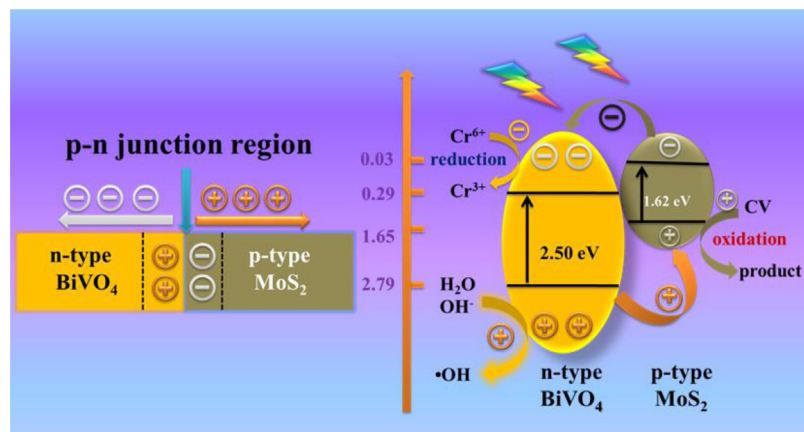


**Fig. 10.** The p-n heterojunction photocatalyst formation model and the mechanism of photocatalysis of p-n heterojunction photocatalyst.

On the basis of the above-described experimental result and discussion, the photocatalysis mechanism of p-n heterojunction photocatalyst and the schematic drawing of electron–hole separation process are illustrated in Fig. 10.

#### 4. Conclusions

In summary, we developed a facile in-situ hydrothermal method to synthesize p-n heterojunction photocatalyst n-BiVO<sub>4</sub>@p-MoS<sub>2</sub> with core–shell structure, and MoS<sub>2</sub> shell thickness was easily tuned by varying the concentration of MoS<sub>2</sub> precursor. The BiVO<sub>4</sub>@MoS<sub>2</sub> heterojunction exhibited the hight photocatalytic reduction of Cr<sup>6+</sup> and oxidation of CV activities, which could be attributed to the suppression of charge recombination, the high specific surface area and strong adsorption ability toward the pollutant molecule, and the enhanced light absorption of BiVO<sub>4</sub>@MoS<sub>2</sub>. Furthermore, 12 intermediates, mostly substituted benzenes and small molecular weight alcohols, were identified by GC-MS in the photocatalytic oxidation of CV process. The present study will benefit the development of the new p-n heterojunction photocatalysts with core–shell structure and may be of great importance to meet the environmental demands in the future.

#### Acknowledgements and note

The authors greatly acknowledge the National Natural Science Foundation of China (No. 51578279 and 51278242), the Natural Science Foundation of Jiangsu Province (BK2012732), and the Shanghai Tongji Gao Tingyao Environmental Science & Technology Development Foundation (STGEF).

The authors thank Dr. Li H. (Department of Plant, Soil and Microbial Sciences, Michigan State University) for his great help at language modification and composition suggestion, Dr. Wu H.-W. (National Laboratory of Solid State Microstructures & Department of Physics, Nanjing University), and Dr. Yuan L. (State Key Laboratory of Inorganic Synthesis and Preparative Chemistry, College of Chemistry, Jilin University) for helpful discussions. W. Zhao and Y. Liu contributed equally to this work (co-first author).

#### Appendix A. Supplementary data

Supplementary data associated with this article can be found, in the online version, at <http://dx.doi.org/10.1016/j.apcatb.2015.12.023>.

#### References

- [1] T. Liu, B. Li, Y. Hao, F. Han, L. Zhang, L. Hu, *Appl. Catal. B* 165 (2015) 378–388.
- [2] H.F. Cheng, T. Kamegawa, K. Mori, H. Yamashita, *Angew. Chem. Int. Ed.* 53 (2014) 2910–2914.
- [3] C. Cui, Y. Wang, D. Liang, W. Cui, H. Hu, B. Lu, S. Xu, X. Li, C. Wang, Y. Yang, *Appl. Catal. B* 158 (2014) 150–160.
- [4] Z.G. Zou, J.H. Ye, K. Sayama, H. Arakawa, *Nature* 414 (2001) 625–627.
- [5] H.M. Chiu, T.H. Yang, Y.C. Hsueh, T.P. Peng, J.M. Wu, *Appl. Catal. B* 163 (2015) 156–166.
- [6] D.Q. Zhang, M.C. Wen, S.S. Zhang, P.J. Liu, W. Zhu, G.S. Li, H.X. Li, *Appl. Catal. B* 147 (2014) 610–616.
- [7] X. Bai, R. Zong, C. Li, D. Liu, Y. Liu, Y. Zhu, *Appl. Catal. B* 147 (2014) 82–91.
- [8] W.I.F. David, I.G. Wood, *J. Phys. C: Solid State Phys.* 16 (1983) 5149.
- [9] K. Hirota, G. Komatsu, M. Yamashita, H. Takemura, O. Yamaguchi, *Mater. Res. Bull.* 27 (1992) 823–830.
- [10] Y. Zhao, Y. Xie, X. Zhu, S. Yan, S.X. Wang, *Chem. Eur. J.* 14 (2008) 1601–1606.
- [11] L. Zhang, D.R. Chen, X.L. Jiao, *J. Phys. Chem. B* 110 (2006) 2668–2673.
- [12] R.G. Li, F.X. Zhang, D.G. Wang, J.X. Yang, M.R. Li, J. Zhu, X. Zhou, H.X. Han, C. Li, *Nat. Commun.* 4 (2013) 1432.
- [13] S. Gu, W. Li, F. Wang, S. Wang, H. Zhou, H. Li, *Appl. Catal. B* 170 (2015) 186–194.
- [14] S.M. Thalluri, S. Hernández, S. Bensaid, G. Saracco, N. Russo, *Appl. Catal. B* 180 (2016) 630–636.
- [15] P.M. Rao, L. Cai, C. Liu, I.S. Cho, C.H. Lee, J.M. Weisse, P. Yang, X. Zheng, *Nano Lett.* 14 (2014) 1099–1105.
- [16] H. Li, Y. Sun, B. Cai, S. Gan, D. Han, L. Niu, T. Wu, *Appl. Catal. B* 170 (2015) 206–214.
- [17] D.K. Zhong, S. Choi, D.R. Gamelin, *J. Am. Chem. Soc.* 133 (2011) 18370–18377.
- [18] Y.N. Huo, X.F. Chen, J. Zhang, G.F. Pan, J.P. Jia, H.X. Li, *Appl. Catal. B* 148 (2014) 550–556.
- [19] W. Zhao, Y. Guo, S. Wang, H. He, C. Sun, S. Yang, *Appl. Catal. B* 165 (2015) 335–343.
- [20] W.Z. Wang, X.W. Huang, S. Wu, Y.X. Zhou, L.J. Wang, H.L. Shi, Y.J. Liang, B. Zou, *Appl. Catal. B* 134 (2013) 293–301.
- [21] E.S. Kim, H.J. Kang, G. Magesh, J.Y. Kim, J.W. Jang, J.S. Lee, *ACS Appl. Mater. Interfaces* 6 (2014) 17762–17769.
- [22] C. Lv, G. Chen, J. Sun, Y. Zhou, S. Fan, C. Zhang, *Appl. Catal. B* 179 (2015) 54–60.
- [23] C.J. Li, P. Zhang, R. Lv, J.W. Lu, T. Wang, S.P. Wang, H.F. Wang, J.L. Gong, *Small* 9 (2013) 3951–3956.
- [24] C.J. Li, S.P. Wang, T. Wang, Y.J. Wei, P. Zhang, J.L. Gong, *Small* 10 (2014) 2783–2790.
- [25] X. Gao, H.B. Wu, L. Zheng, Y. Zhong, Y. Hu, X.W.D. Lou, *Angew. Chem. Int. Ed.* 126 (2014) 6027–6031.
- [26] X. Yu, R. Du, B. Li, X. An, H. Liu, J. Qu, Y. Zhang, *Appl. Catal. B* (2015), <http://dx.doi.org/10.1016/j.apcatb.2015.09.003>.
- [27] Y.J. Yuan, Z.T. Yu, Y.H. Lu, X. Chen, W.G. Tu, Z.G. Ji, Z.G. Zou, *Appl. Catal. B* 181 (2016) 16–23.
- [28] W.J. Zhou, Z.Y. Yin, Y.P. Du, X. Huang, Z.Y. Zeng, Z.X. Fan, H. Liu, J.Y. Wang, H. Zhang, *Small* 9 (2013) 140–147.
- [29] H.L. Li, K. Yu, X. Lei, B.J. Guo, H. Fu, Z.Q. Zhu, *J. Phys. Chem. C* 119 (2015) 22681–22689.
- [30] F. Meng, J. Li, S.K. Cushing, M. Zhi, N. Wu, *J. Am. Chem. Soc.* 135 (2013) 10286–10289.
- [31] K. Yu, S. Yang, C. Liu, H. Chen, H. Li, C. Sun, S.A. Boyd, *Environ. Sci. Technol.* 46 (2012) 7318–7326.
- [32] C.B. Liu, L.L. Wang, Y.H. Tang, S.L. Luo, Y.T. Liu, S.Q. Zhang, Y.X. Zeng, Y.Z. Xu, *Appl. Catal. B* 164 (2015) 1–9.
- [33] K.P. Parmar, H.J. Kang, A. Bist, P. Dua, J.S. Jang, J.S. Lee, *ChemSusChem* 5 (2012) 1926–1934.

- [34] Z.Q. He, Y.Q. Shi, C. Gao, L.N. Wen, J.M. Chen, S. Song, *J. Phys. Chem. C* 118 (2013) 389–398.
- [35] B. Stypula, J. Stoch, *Corros. Sci.* 36 (1994) 2159–2167.
- [36] S.F. Chen, S.J. Zhang, W. Liu, W. Zhao, *J. Hazard. Mater.* 155 (2008) 320–326.
- [37] M.R. Hoffmann, S.T. Martin, W.Y. Choi, D.W. Bahnemann, *Chem. Rev.* 95 (1995) 69–96.
- [38] X. Fu, M. Xie, P. Luan, L. Jing, *ACS Appl. Mater. Interfaces* 6 (2014) 18550–18557.
- [39] D.K. Ma, M.L. Guan, S.S. Liu, Y.Q. Zhang, C.W. Zhang, Y.X. He, S.M. Huang, *Dalton Trans.* 41 (2012) 5581–5586.
- [40] K. Ji, J. Deng, H. Zang, J. Han, H. Arandiyan, H. Dai, *Appl. Catal. B* 165 (2015) 285–295.
- [41] W. Ho, J.C. Yu, J. Lin, J.G. Yu, P.S. Li, *Langmuir* 20 (2004) 5865–5869.
- [42] X. Zong, H.J. Yan, G.P. Wu, G.J. Ma, F.Y. Wen, L. Wang, C. Li, *J. Am. Chem. Soc.* 130 (2008) 7176–7177.
- [43] X.F. Zhou, C. Hu, X.X. Hu, T.W. Peng, J.H. Qu, *J. Phys. Chem. C* 114 (2010) 2746–2750.
- [44] Y.Q. Yang, G.K. Zhang, S.J. Yu, X. Sheng, *Chem. Eng. J.* 162 (2010) 171–177.
- [45] Y.Y. Li, J.S. Wang, H.C. Yao, L.Y. Dang, Z.J. Li, *J. Mol. Catal. A: Chem.* 334 (2011) 116–122.
- [46] C. Tang, E. Liu, J. Wan, X. Hu, J. Fan, *Appl. Catal. B* 181 (2015) 707–715.
- [47] H. Yu, X. Li, X. Quan, S. Chen, Y. Zhang, *Environ. Sci. Technol.* 43 (2009) 7849–7855.
- [48] F.T. Li, Q. Wang, X.J. Wang, B. Li, Y.J. Hao, R.H. Liu, D.S. Zhao, *Appl. Catal. B* 150 (2014) 574–584.
- [49] L. Yang, S. Luo, Y. Li, Y. Xiao, Q. Kang, Q. Cai, *Environ. Sci. Technol.* 44 (2010) 7641–7646.
- [50] H. Xu, H. Li, C. Wu, J. Chu, Y. Yan, H. Shu, Z. Gu, *J. Hazard. Mater.* 153 (2008) 877–884.
- [51] J. Kim, C.W. Lee, W. Choi, *Environ. Sci. Technol.* 44 (2010) 6849–6854.
- [52] H.F. Cheng, B.B. Huang, Y. Dai, X.Y. Qin, X.Y. Zhang, *Langmuir* 26 (2010) 6618–6624.